

A robust numerical method for the generation and propagation of periodic finite-amplitude internal waves in natural waters using high-accuracy simulations

Pierre Lloret¹, Peter J. Diamessis¹, Marek Stastna², and Greg N. Thomsen³

¹School of Civil and Environmental Engineering, Cornell University, Ithaca, NY, USA

²Department of Applied Mathematics, University of Waterloo, Waterloo, ON, Canada

³Wandering Wakhs Research, Austin, TX, USA

Correspondence: Pierre Lloret (pel62@cornell.edu)

Abstract. The design and implementation of boundary conditions for the robust generation and simulation of periodic finite-amplitude internal waves is examined in a quasi two-layer continuous stratification using a spectral-element-method-based incompressible flow solver. The commonly-used Eulerian approach develops spurious, and potentially catastrophic, small-scale numerical features near the wave-generating boundary in a nonlinear stratification when the parameter $A/(\delta c)$ is sufficiently larger than unity ; A , δ are measures of the maximum wave-induced vertical velocity and pycnocline thickness, respectively, and c is the linear wave propagation speed. To this end, an Euler-Lagrange approach is developed and implemented to generate robust high-amplitude periodic deep-water internal waves. Central to this approach is to take into account the wave-induced (isopycnal) displacement of the pycnocline in both the vertical and (effectively) upstream directions. With amplitudes not restricted by the limits of linear theory, the Euler-Lagrange-generated waves maintain their structural integrity as they propagate away from the source. The advantages of the high-accuracy numerical method, whose minimal numerical dissipation cannot damp the above near-source spurious numerical features of the purely Eulerian case, can still be preserved and leveraged further along the wave propagation path through the robust reproduction of the nonlinear adjustments of the waveform. The near-and-far-source robustness of the optimized Euler-Lagrange approach is demonstrated for finite-amplitude waves in a sharp quasi two-layer continuous stratification representative of seasonally stratified lakes. The findings of this study provide an enabling framework for two-dimensional simulations of internal swash zones driven by well-developed nonlinear internal waves and, ultimately, the accompanying turbulence-resolving three-dimensional simulations.

1 Introduction

Internal swash zones (ISZs) (Emery and Gunnerson, 1973; Woodson, 2018) are regions which develop along sloping oceanic boundaries through the action of periodically incident internal waves (IWs) in a manner analogous to a surface swash zone on the beach, albeit at slower timescales ($O(10)$ minutes) or longer) and over longer wavelengths ($O(1)$ km) or longer) (Cowen et al., 2003; Elfrink and Baldock, 2002). In ISZs, energy can flux downscale to turbulence effectively either through shear or convective instabilities in the IW interior, similarly to spilling or plunging breaker waves on the ocean surface (Cowen et al.,

2003; Ting and Kirby, 1996), or through the turbulent boundary layer established through the interaction of the IW-induced current with the seafloor (Zulberti et al., 2022). In the latter context, particularly strong turbulence can be generated in the form of a near-bottom turbulent wake due to boundary layer separation associated with the along-bed wave-induced adverse pressure gradient induced by either internal bores or internal solitary waves (Hosegood et al., 2004; Boegman and Stastna, 2019). The above turbulence-generation mechanisms presumably conspire to drive significant boundary-interior exchange (McPhee-Shaw and Kunze, 2002; MCPhee-Shaw, 2006), i.e., the exchange of water between the boundary layer and the stratified interior, which effectively drives mixing in the relatively less active stratified water-body interior (McPhee-Shaw and Kunze, 2002; Boegman and Ivey, 2009). The periodic shoaling and breaking of the above IWs in shallow environments, like continental shelves or slopes, has a direct impact on the internal thermal equilibrium and biogeochemistry of the water column (Woodson, 2018). The periodically on-slope incident IWs are important in the transfer of mass, whether transporting nutrients and plankton toward the surface in the inner shelf (Omand et al., 2015) or whether ejecting bottom boundary layer sediments as high as 40 meters into the water column during a strong vertical updraft event associated with the passage of a nonlinear internal wave of depression over the slope (Cheriton et al., 2016). A similar class of long IW-driven phenomena, of comparable biogeochemical importance, also occur on the slopes of lakes (Thorpe, 1998; Wuest and Lorke, 2003) and have served as the primary motivator of the research presented here.

The leading-order component of the periodic wave field forcing of an ISZ consists of lower vertical mode IWs whose wavelength is $O(50 - 100)$ longer than the water column depth, namely in the form of oceanic internal tidal waves or the basin-scale internal seiche of a lake (Emery and Gunnerson, 1973; Nash et al., 2004; Stevens et al., 2005; Martini et al., 2013; Lemckert and Imberger, 1998). In the latter case, the internal seiche is further associated with a lower horizontal mode associated with the longer dimension of the lake. Such long waves are commonly expected to be represented, with sufficient fidelity, through the use of linear IW theory (Stastna, 2022) at, nonetheless, values of *finite wave amplitude*. Frequently, higher-frequency/shorter-wavelength highly nonlinear features, such as turbulent/undular bores or internal solitary waves (Stastna, 2022) may be embedded within the longer incident IW (Hosegood et al., 2004; Lucas and Pinkel, 2022; Thorpe et al., 1996).

The primary objective of this paper is the development of a robust numerical method for the generation and subsequent development of the longer component of the deep-water wave-forcing at *finite amplitude*. The generated wave should have an amplitude that is not constrained by the limits of linear theory. Practically, this corresponds to wave-induced maximum isopycnal displacements that are at least 5% of the total water column depth. The wave should also remain sufficiently *robust near the source* and, with an equal degree of robustness, *nonlinearly adjustment of its waveform* as it propagates along the waveguide. In this regard, central to this paper's scope is that the background stratification extend beyond an uniform density gradient (Taylor, 1993) and is actually subject to variation in the vertical, as characterized by the presence of a distinct pycnocline which is commonly a close approximation of the in-situ background profiles in the stratified ocean or lakes. Finally, an additional essential ingredient of this study, is that a high-accuracy discretization is used, specifically a nodal spectral element method (Diamantopoulos et al., 2022). The particular discretization technique enables the optimal resolution of the generated waves, their nonlinear adjustments away from the source and ultimately (though not explicitly considered here) the associated instabilities/turbulence upon encounter of the waves with the slope.

In the laboratory, one approach to generate periodic long internal IWs is by tilting and releasing the actual laboratory tank (Boegman et al., 2005): the resulting horizontal standing wave is a lab-scale surrogate of the basin-scale internal seiche generated in a long stratified lake in response to a strong wind event (Boegman, 2009). An equivalent type of horizontal standing wave may be generated in a numerical simulation within a long rectangular computational domain by using an initial condition consisting of a tilted pycnocline (Grace et al., 2019). One issue with the tilting-based wave-generation approach may be that it immediately produces finite velocities across the whole domain/tank, when one would prefer waves propagating into an initially quiescent slope region. In many cases, the standing wave will breakdown into a propagating wave train (Grace et al., 2019).

An alternative, more flexible and effectively more controllable, wave generation approach involves introducing a form deep-water (far from the slope) oscillatory wave-excitation. Such an approach would ideally allow a *sufficiently long propagation distance in uniform depth waters*, prior to the wave encountering the slope, which permits the generated IW to undergo any required nonlinear adjustments. To this end, in the deep-water section of a laboratory tank, a horizontally oscillating paddle (Wallace and Wilkinson, 1988; Nakayama and Imberger, 2010; Ghassemi et al., 2022), a vertically oscillating semi-cylinder (Moore et al., 2016) or an array of plates vertically stacked on an eccentric camshaft (Mercier et al., 2010, 2013) have been used. It is worth noting that all the above experimental studies generated relatively short waves, as represented by values of aspect ratio λ/H and non-dimensional amplitude η_{max}/H ; λ , η_{max} and H are the IW horizontal wavelength, IW-induced maximum isopycnal displacement and water depth, respectively. Reported directly, or inferred, values of λ/H and η_{max}/H lie in the range [2, 12.5] and [0.0075, 0.2] respectively, in the above laboratory studies wherever directly identifiable or inferable. Such a maximum pycnocline displacement range corresponds to a wave Froude number, $Fr = U_{max}/c$, of [0.02, 0.35]; U_{max} and c are the maximum wave-induced horizontal current and wave propagation speed.

The high-order-accuracy turbulence-resolving fully nonlinear and non-hydrostatic three-dimensional simulations of Winters (2015) are one of the few computational studies so far which has considered the generation and incidence of a periodic long wave and on a, relatively steep, slope. The wave aspect ratio and wave Froude number can be inferred as $\lambda/H = 48$ and $Fr = 0.1385$. Note that the work of Winters considered only a uniform background stratification. Moreover, his generated waves were allowed a distance less than one prescribed wavelength from the source to propagate until the slope most likely precluding any deep-water nonlinear adjustments of the waveform.

To the authors best knowledge, the only other computational study which has examined the periodic generation, the propagation away from the source over at least one wavelength and the incidence of long internal waves on a slope is the two-dimensional investigation by Dauhajre et al. (2021). The wave aspect ratios considered in this study are high and can be inferred as residing in the range [50, 400], while noting the very small ratio of computational domain depth to length. The wave based Froude number values considered are in the range [0.05, 0.4]. Furthermore, the subset of simulations that use a two-layer stratification (and not a linear one) have a thick pycnocline and focus on an aspect ratio of $\lambda/H = 200$ and a wave based Froude number between 0.1 and 0.2. Note also the curvature of the density profile at the base of the pycnocline is reduced by introducing a weakly stratified layer below. The numerical dissipation inherently built into the parameterizations of

the regional ocean modeling code (ROMS) used in this study could also effectively damp any spurious numerical features near the wave-generating deep-water boundary.

Note that the studies of Masunaga et al. (2015, 2016); Walter et al. (2012) also considered a non-uniform stratification but positioned the wave-generating source only a fraction of the target wavelength from the slope. The generated waves, therefore, were not afforded an adequate propagation distance to undergo any nonlinear adjustments before encountering the slope. Additionally, per this paper’s focus on periodic IW simulation with high-accuracy methods and high resolution, the nesting-based robust mode-1 long internal tide generation within a regional-scale nonhydrostatic model (Rogers et al., 2019) is not pertinent to the scope of this study as it relies on low-pass filtering and sponge layers.

The laboratory and computational studies discussed above consider generated waves that may be deemed as either short or long. Even when high-accuracy/resolution numerical methods are derived and efficiently implemented on a state-of-the-art high-performance computing platform, a computational study aiming to sufficiently resolve instability/turbulence formation due to sufficiently high-amplitude waves over a limited number cycles of an ISZ is practically limited to a wave aspect ratio in the range [40, 50]. This is the aspect ratio regime accessed by the work of Winters (Winters, 2015), which is however limited to a linear stratification. The choice of a linear stratification effectively shielded this study from the challenges that emerge when forcing internal waves in a pycnocline-dominated stratification profile. As will be demonstrated later in this paper, the generation of high-amplitude periodic internal waves in more general, nonlinear, stratifications for waves operating in this intermediate aspect ratio range is confronted with non-trivial error if commonly used deep-water forcing approaches, such as those employed by Winters and Dauhajre et al., are actually employed. The minimal numerical dissipation of a high-order-accuracy numerical method can allow this error to grow substantially. The stability of the simulation can thus be effectively undermined, and one can no longer leverage the high-accuracy of the method for representing nonlinear wave adjustments in deeper-water and the finer-scale features once the slope is reached.

Thus from a computational point of view a relatively simple technique for generating larger-amplitude IWs for general stratifications in deep water is highly desirable. This is often achieved by choosing a form of boundary conditions at the boundary away from the slope region. For most field-relevant stratifications, a pycnocline dominates the stratification, and the vertical motion of then pycnocline is the clearest manifestation of internal waves. Historically, descriptions of internal waves typically built on a linearized theory and the literature has examples of two different choices for the vertical coordinate: one which uses the physical coordinate z , and one which uses the upstream height of each isopycnal (and more concretely, the upstream height of the dominant pycnocline) (Gear and Grimshaw, 1983; Yih, 1977). Since the former uses the physical coordinates, it is usually labelled as the *Eulerian* theory of linear internal waves. The latter, in contrast, is labelled the *Euler-Lagrange* theory because the horizontal coordinate is the physical coordinate x , while the vertical coordinate is the upstream coordinate, often written as $y = z - \eta(x, z, t)$ where η is the the isopycnal displacement. Both the Eulerian (Lamb and Yan, 1996) and Euler-Lagrange theories (Gear and Grimshaw, 1983) have been used as a basis for multi-scale asymptotic expansions that extend the wave description to small, but finite amplitude waves (i.e. weak nonlinearity), and waves of finite wavelength (i.e. weak dispersion). These lead to model equations in the Korteweg-de-Vries family. The use of the upstream isopycnal height has found general use in the description of stratified flow, in both the classical (Yih, 1977) and modern (Stastna, 2022)

contexts. In the simulation context, the desire to generate finite amplitude waves in a situation with a strong pycnocline implies that forcing methodologies based on Eulerian, linear wave theory may not yield robust results. The Euler-Lagrange theory offers an alternative, if algebraically more complex, development pathway.

130 In this paper, by following an Eulerian and an Euler-Lagrange approach (Turkington et al., 1991; Gear and Grimshaw, 1983), different types of time-dependent periodic wave-generating boundary conditions are derived with a particular emphasis on the subtleties associated with a continuous two-layer background stratification. The efficacy of each approach in generating a robust deep-water periodic finite-amplitude IW train and enabling any nonlinear adjustments of the wave-train is thereafter assessed.

135 2 Problem set-up and model formulation

2.1 Problem geometry

The canonical flow examined in this paper is the propagation of a two-dimensional finite amplitude periodically forced internal wave in a quasi two-layer continuous stratification. The computational domain is a two-dimensional rectangle of dimensions $L \times H$ and is stratified in the vertical direction z with a vertically varying buoyancy frequency $N(z)$ where

$$140 \quad N^2(z) \equiv -\frac{g}{\rho_0} \frac{d\bar{\rho}}{dz}. \quad (1)$$

Restricting one's focus to the Boussinesq approximation, the total density is decomposed as the addition of a reference density ρ_0 , a stratification $\bar{\rho}$ and a perturbation ρ' (Kundu et al., 2008):

$$\rho(\mathbf{x}, t) = \rho_0 + \bar{\rho}(z) + \rho'(\mathbf{x}, t) \text{ with } \rho' \ll \bar{\rho} \ll \rho_0. \quad (2)$$

The quasi two-layer continuous stratification $\bar{\rho}$ (Fig. 1, left panel) is defined by:

$$145 \quad \bar{\rho}(z) = -\frac{\rho_0 N_0^2 \delta}{g} \tanh\left(\frac{z - z_p}{\delta}\right), \quad (3)$$

where $\rho_0 N_0^2 \delta / g$ is a measure of the density difference across the pycnocline, N_0 is a reference buoyancy frequency equal to the peak value of $N(z)$ in the water column, δ is a measure of the pycnocline thickness and z_p is the position of the pycnocline's center.

The finite amplitude internal wave, of wavenumber k and angular frequency ω , is generated through a forcing implemented within the left boundary conditions. Details on the exact derivation of the deep water boundary conditions will be covered in Section 3.

150

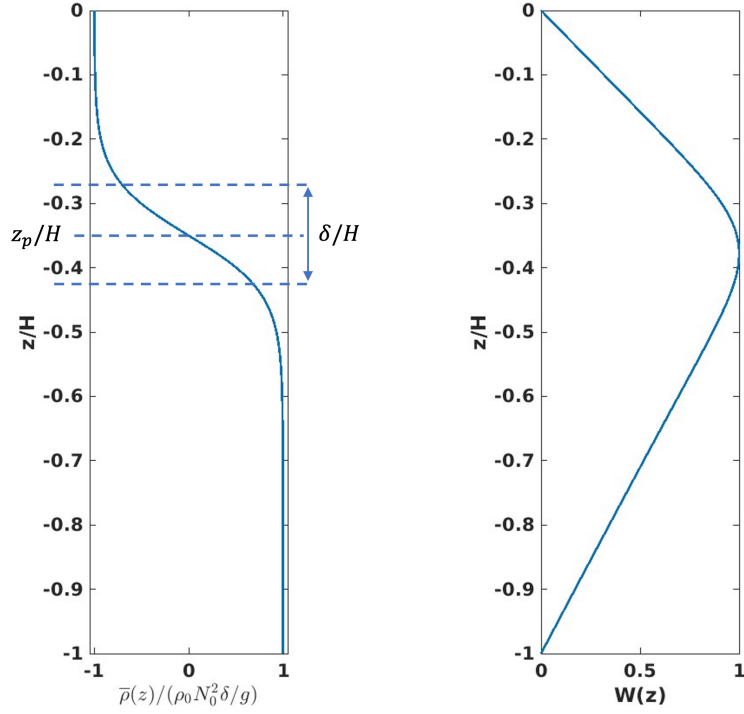


Figure 1. **Left:** A two layer continuous stratification $\bar{\rho}$, defined by its density jump $2\rho_0 \frac{N_0^2 \delta}{g}$, its position z_p and its thickness δ . **Right:** Corresponding vertical structure eigenfunction $W(z)$ which is the solution to the eigenvalue problem Eq. (16).

2.2 Governing equations

The governing equations for the problem are the incompressible Navier-Stokes equations (INSE) under the Boussinesq approximation, written as:

$$155 \quad \frac{\partial \mathbf{u}}{\partial t} = -\mathbf{u} \cdot \nabla \mathbf{u} - \frac{g}{\rho_0} \rho' \mathbf{k} - \frac{1}{\rho_0} \nabla p' + \nu \nabla^2 \mathbf{u}, \quad (4)$$

$$\frac{\partial \rho'}{\partial t} = -\mathbf{u} \cdot \nabla \rho + \kappa \nabla^2 \rho', \quad (5)$$

$$\nabla \cdot \mathbf{u} = 0. \quad (6)$$

The simulations reported here will be limited to two dimensions on the (x, z) plane. Therefore \mathbf{u} will be limited to its two components (u, w) . Furthermore ρ' is the density perturbation as defined in Eq. (2) and p' is the pressure perturbation, defined as the deviation from the hydrostatic pressure. It is important to note that the hydrostatic balance between $\bar{p}(z)$ and the corresponding background pressure field has been subtracted from Eq. (5). Here \mathbf{k} is the unit vector in the positive direction, ν and κ are the constant kinematic viscosity and mass diffusivity and g is the gravitational constant.

At the deep water wave-generating boundary condition Dirichlet time dependent boundary conditions are enforced as:

$$\mathbf{u}(x=0, z, t) = f_{\mathbf{u}}(z, t) = \begin{pmatrix} f_u(z, t) \\ f_w(z, t) \end{pmatrix} \quad (7)$$

$$\rho(x=0, z, t) = f_{\rho}(z, t), \quad (8)$$

where f_u , f_w and f_{ρ} will be explicitly described in Sec. 3 for the different forcing approaches considered here. A free-slip boundary condition is prescribed for the velocity field along all other boundaries and the density is subject to a boundary condition of zero diffusive flux:

$$\frac{\partial \rho}{\partial n} = \nabla \rho \cdot \mathbf{n} = 0. \quad (9)$$

2.3 Wave-based dimensionless parameters

The definition of the wave-based Reynolds number Re_w is given by

$$Re_w \equiv \frac{\lambda c}{\nu}, \quad (10)$$

where λ is the associated wavelength and $c = \omega/k$ the wave-speed of the prescribed wave. The particular wave-based Reynolds number is independent of the wave amplitude and quantifies the strength of viscous effects during the time required for the wave to propagate a distance of one wavelength λ .

The wave aspect ratio λ/H is a metric used to describe how long the wave is relatively to the water depth. Additionally, in the context of this study, it effectively represents the upstream variation of wave-induced flow fields at the wave-generating deep-water boundary which then determines which variant of an Euler-Lagrange-approach must be used.

The Froude number quantifies the strength of nonlinear effects within the wave against the restoring effect of buoyancy and is defined as:

$$Fr \equiv \frac{U_0}{c}, \quad (11)$$

where U_0 is the maximum-wave induced horizontal fluid velocity.

2.4 Numerical method

The numerical method used to generate the simulation data sets examined in this paper is a high-order continuous-Galerkin numerical method, originally developed for the simulation of non-linear, non-hydrostatic internal waves and turbulence in

long computational domains with complex bathymetry. The time discretization is semi-implicit and relies on a third order stiffly stable scheme (Karniadakis et al., 1991). The spatial discretization is based on the nodal spectral element method. Such a discretization enables robust wave propagation against numerical dispersion and diffusion effects, a highly accurate
 190 representation of complex geometries and a flexibility in localized resolution, namely the across pycnocline. Details on the discretization of the Pressure Poisson equation, and its Laplacian operator (which are directly applicable to the viscous term treatment) may be found in Appendix A. More details on the numerical model may be found elsewhere (Diamantopoulos et al., 2022).

Such a temporal discretization leads to a Poisson equation for the pseudopressure \bar{p} at time level $(n + 1)$:

$$195 \quad \nabla^2 \bar{p}^{n+1} = \nabla \cdot \left(-\frac{\hat{\mathbf{u}}}{\Delta t} \right), \quad (12)$$

where \bar{p} is defined as:

$$\int_{t_n}^{t_{n+1}} \nabla p' dt = \Delta t \nabla \bar{p}^{n+1}. \quad (13)$$

For the temporal discretization used in this work, the appropriate boundary conditions for the pressure Poisson equation are taken from Karniadakis et al. (1991). The particular boundary condition is augmented by a term which accounts for the time
 200 dependence of the wave-generating boundary condition the boundary-normal velocity:

$$\frac{\partial \bar{p}}{\partial n} = \mathbf{n} \cdot \left[\sum_{q=0}^{J_e-1} \beta_q \mathbf{N}(\mathbf{u}^{n-q}) + \nu \beta_q \mathbf{L}(\mathbf{u}^{n-q}) + \frac{\partial f_{\mathbf{u}}(z, t)}{\partial t} \right] \quad (14)$$

where coefficient β_q correspond to a third-order stiffly stable scheme, \mathbf{N} and \mathbf{L} are the nonlinear and linear operators, respectively, (Karniadakis et al., 1991).

3 Deep water wave-generating boundary conditions

205 The generation of finite-amplitude periodic internal waves is a key component of this study. To this end, we examine the spatio-temporal structure of the generated wave, as prescribed by linear theory, which is introduced into the computational domain in the form of time-dependent, vertically-variable Dirichlet conditions at the deep-water boundary.

3.1 Internal wave vertical structure: mathematical descriptions

The fluid's top and bottom boundaries naturally confine the propagation of internal waves so that it occurs in the horizontal
 210 direction, along a waveguide formed by the naturally occurring density stratification as shown in Fig. 2. This density stratification, which only varies in the z direction, is often dominated by a region of rapid change (the so-called pycnocline) and it is the up and down motion of this pycnocline that is essential for an accurate description of wave motion.

Mathematically, internal waves can be represented as a separation of variables solution with a fixed, or standing wave, structure in the vertical and a propagating waveform (a plane wave in the linear theory) in the horizontal. If we choose the

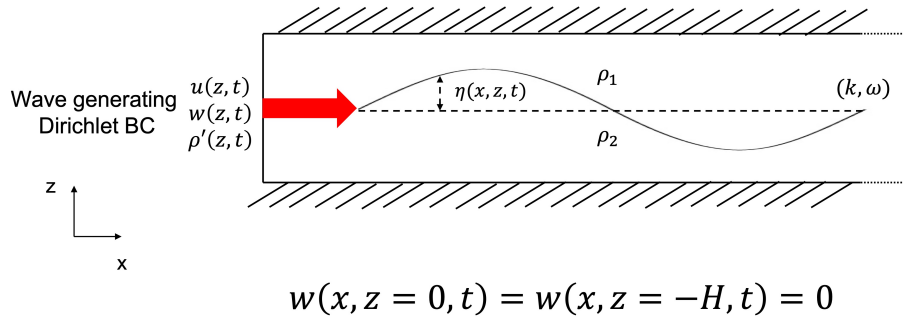


Figure 2. Schematic of the generation of a mode-1 wave in the wave guide analogy using time-dependent boundary conditions for a two-layer stratification, highlighting the pycnocline displacement η .

215 propagation direction to be from left to right, and assume the waves to be periodic in x and t , the vertical component of velocity will have the form:

$$w(\mathbf{x}, t) = W(z) \exp[i(kx - \omega t)]. \quad (15)$$

The equation governing the vertical structure may be derived by linearizing the stratified Euler equations under the Boussinesq approximation (which in turn result from dropping the viscous/diffusive terms in Eq. (4)), performing a series of algebraic
 220 manipulations to leave an equation for w only, and introducing the wave ansatz above. The buoyancy frequency profile $N(z)$ is assumed given, and for the scope of this paper we are neglecting any form of background shear current. $W(z)$ then becomes the solution of the following linear eigenvalue problem (Gerkema and Zimmerman, 2008), for either ω or k with the other parameter assumed specified:

$$\frac{d^2 W}{dz^2} + k^2 \frac{N^2(z) - \omega^2}{\omega^2} W = 0. \quad (16)$$

225 Both top and bottom boundaries are assumed impermeable such that:

$$W(0) = W(-H) = 0. \quad (17)$$

For a given wave number k , an infinite number of eigenfunctions $W_n(z)$ with their corresponding eigenvalues ω_n exist, each one representing a different vertical mode (i.e. mode-1 does not cross zero in the interior of the fluid, mode-2 crosses zero once in the interior of the fluid, etc). Therefore the general solution $w(\mathbf{x}, t)$ can be represented by a superposition of such
 230 modes, using arbitrary constants $a_n \in \mathbb{C}$:

$$w(\mathbf{x}, t) = \sum_n W_n(z) [a_n \exp(i(kx - \omega_n t))]. \quad (18)$$

Details regarding the derivation of the solution in the linear stratification case, which are pertinent to the discussion in Section 4, are provided in Appendix B.

3.2 Eulerian approach

235 The above description computes w as a function of a *fixed coordinate system*. This is often called the “lab frame” and the theory is labelled as *Eulerian* (Kundu et al., 2008). In this first approach to generate a finite amplitude periodic IW, a two-dimensional perturbation field (u_E, w_E, ρ'_E) is constructed from the solution of the eigenvalue problem for $W(z)$ via the following set of manipulations of the linearized, stratified Euler equations under the Boussinesq approximation:

$$\frac{\partial \mathbf{u}_E}{\partial t} = -\frac{g}{\rho_0} \rho'_E \mathbf{k} - \frac{1}{\rho_0} \nabla p', \quad (19)$$

240
$$\frac{\partial \rho'_E}{\partial t} = -w_E \frac{\partial \bar{\rho}}{\partial z}, \quad (20)$$

$$\nabla \cdot \mathbf{u}_E = 0. \quad (21)$$

As mentioned above, such an approach can be considered as Eulerian since we are looking at the evolution in time of the wave induced velocity and density fields from a fixed frame of reference. Without a loss of generality, since the chosen equations are linear, only a mode-1 wave will be considered, corresponding to the smallest wave number possible. Following the stratified waveguide analogy (see Section 3.1), and multiplying the result by an arbitrary scaling factor A , effectively a
 245 measure of wave amplitude, the resulting w_E perturbation is:

$$w_E(x, z, t) = -Ak \cos(kx - \omega t) W(z). \quad (22)$$

Using continuity, Eq. (21), an expression for u_E is derived accordingly:

$$u_E(x, z, t) = A \sin(kx - \omega t) \frac{dW}{dz}. \quad (23)$$

250 Further appealing to the linearized form of the advection-diffusion equation, Eq. (20), the density perturbation ρ'_E is then:

$$\rho'_E(x, z, t) = -\frac{d\bar{\rho}}{dz} \frac{Ak}{\omega} \sin(kx - \omega t) W. \quad (24)$$

The result of the above derivation is a field (u_E, w_E, ρ'_E) , shown in Figs. 3 (a) and 3 (b) at an arbitrary time, of a propagating internal wave solution of the linear Euler equations under the Boussinesq approximation. The approximate fields are two-dimensional in space, x, z , and also depend on time t . They exhibit a separable structure in $x - t$ and the vertical direction
 255 z .

In practice, the approximations are implemented through a Dirichlet boundary condition (see Eqs. (7) and (8)) along a vertical boundary, which we assume to occur at $x = 0$, without any loss of generality.

As a result, the deep-water boundary forcing functions for the Eulerian approach are defined as:

$$f_u^E(z, t) = A \sin(-\omega t) \frac{dW}{dz} \quad (25)$$

260

$$f_w^E(z, t) = -Ak \cos(-\omega t) W(z) \quad (26)$$

$$f_\rho^E(z, t) = -\frac{d\bar{\rho}}{dz} \frac{Ak}{\omega} \sin(-\omega t) W. \quad (27)$$

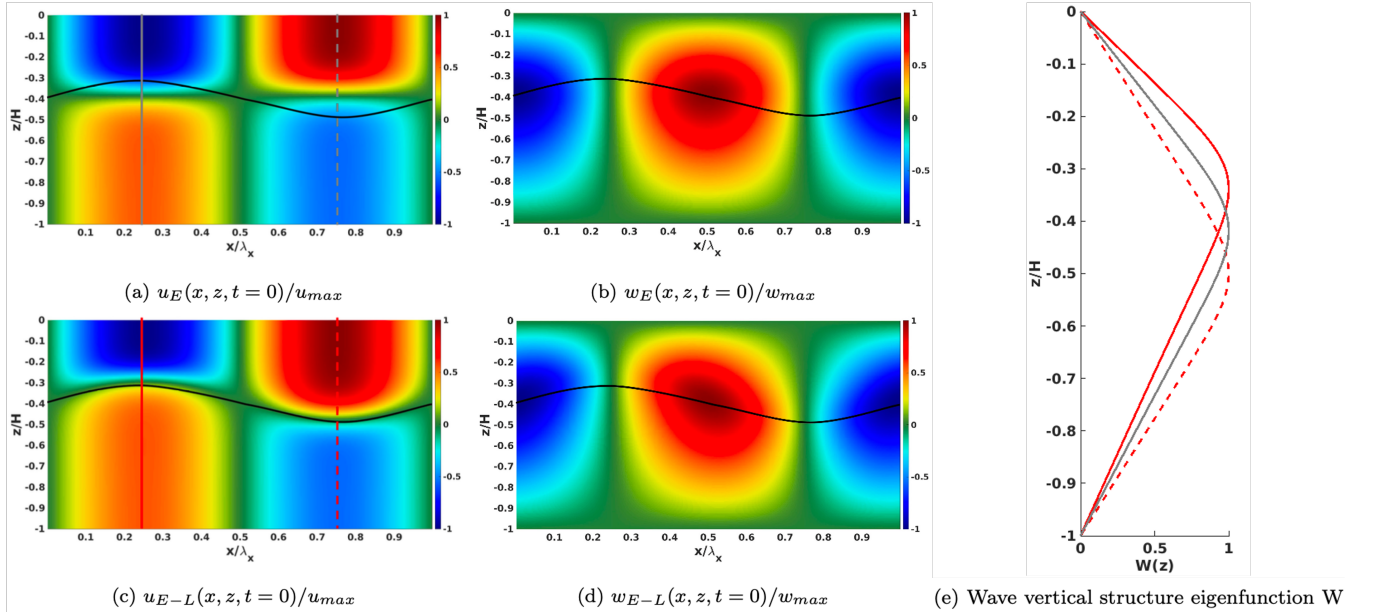


Figure 3. Snapshots of the velocity fields over one wavelength in the Eulerian approach (panels (a) and (b)) and in the Euler-Lagrange approach (panels (c) and (d)) at an arbitrary time $t = 0$ to highlight the spatial wave form. Panel (e) presents the corresponding wave vertical structures at different locations represented as vertical lines in panels (a) and (c).

The displaced pycnocline is represented as a black line. Velocities are normalized with their maximum values.

3.3 Euler-Lagrange approach

265 When the Eulerian approach in Section 3.2 is applied to situations with a sharp pycnocline, a consistent error is observed for all but the smallest and shortest waves (see Section 3.4.2). This disintegration of the generated wave is due to the fact that the

up-and-down motion of the pycnocline is not accounted for in the vertical mode description. A natural way to account for this motion is achieved by introducing the wave induced displacement of the pycnocline. This is measured by the vertical displacement $\eta(x, z, t)$ of the isopycnals (Fig. 2), or isopycnal displacement. Such an approach is labelled as *partially Lagrangian* since
 270 it follows the *vertical* displacement of individual fluid parcels through time. When combined with the usual description in the horizontal, it is labelled as an Euler-Lagrange approach (Gear and Grimshaw, 1983; Turkington et al., 1991).

Introducing the vertical displacement $\eta(x, z, t)$ of the isopycnals allows for a different, more natural description, of the perturbed stratification. Specifically, neglecting the uniform background density ρ_0 for the sake of compactness, the wave-induced density field can be alternatively expressed as,

$$275 \quad \rho(\mathbf{x}, t) = \bar{\rho}(z - \eta(x, z, t)), \quad (28)$$

which signifies that the density at a point is the same as that at an appropriate height far upstream. The density perturbation ρ'_{E-L} can also be rewritten as,

$$\rho'_{E-L} = \bar{\rho}(z - \eta(x, z, t)) - \bar{\rho}(z). \quad (29)$$

Taylor expanding the right hand side shows that ρ'_{E-L} is a polynomial in η with the classical Eulerian description giving
 280 only the first term:

$$\rho'_{E-L} \approx -\eta \frac{d\bar{\rho}}{dz} + \frac{1}{2} \frac{d^2\bar{\rho}}{dz^2} \eta^2. \quad (30)$$

By effectively keeping more terms in the expansion, the efficacy of the deep water forcing is improved significantly. The first term carries a structure representative of the Eulerian approach in Eq. (24). However, from the second derivative of the background density profile in the second term, we can see that Euler-Lagrange effects can be expected to be important for
 285 finite-amplitude waves when the stratification exhibits a sharp pycnocline. Such is exactly the case for the study at hand and the continuous two-layer stratification it uses (see Fig. 1 and Section 3.4.1).

At this juncture, it is worth emphasizing that the inclusion of the second term in the Taylor expansion of Eq. (30) still only provides an approximate solution of the governing equations (both the linear and nonlinear Euler equations) for the input wave field. The purpose of this study is not provide an exact solution in this context, particularly in a nonlinear sense as enabled,
 290 e.g., by the internal-solitary-wave-generating algorithm of Turkington et al. (1991) as implemented in Dunphy et al. (2011). Instead, as will be subsequently be demonstrated, we are aiming for an approximate solution of the linear Euler equations that will drive the deep-water boundary forcing of finite-amplitude waves in a fully nonlinear simulation such that the waves can remain robust both near the source and further along the propagation path when nonlinear effects modify their waveform.

For the quasi two-layer continuous stratification case, an order of magnitude comparison between the two terms in the right-
 295 hand-side of Eq. (30) may be obtained if one uses as characteristic density and length scales the density jump, $\Delta\rho$, across the

pycnocline and the pycnocline thickness, δ . Per Eqs. (34) and (40), as outlined in the next two sections, one may further write out the isopycnal displacement function as:

$$\eta(x, z, t) = A \frac{k}{\omega} r(x, z, t), \quad (31)$$

where A is the previously introduced amplitude factor and $r(x, z, t)$ is a structure function, harmonic in x and t and determined by the eigenfunction $W(z)$ in the vertical, which assumes values in the range $[-1, 1]$. Using the characteristic scales above and Eq. (31), one can show that the ratio of the magnitude of the second term to that of the first one in the right-hand-side of Eq. (30) scales as $(A/\delta)(k/\omega)r(x, z, t)$. Therefore, the strength of the Euler-Lagrange effects becomes important when the parameter $(A/\delta)/(k/\omega) = A/(\delta c)$ is sufficiently larger than unity; here $c = \omega/k$ is the linear phase speed obtained by solving the eigenvalue problem outlined in Sec. 3.1. The particular condition is satisfied for high wave amplitude, small pycnocline thickness and slow wave propagation speeds.

Restricting the scope to vertical mode-1 waves if $A/(\delta c)$, is sufficiently larger than unity, Euler-Lagrange effects also become important when the structure function $r(x, z, t)$ is $O(1)$ over a long enough horizontal length-scale. For very long waves, $\lambda/H \gg 1$, this is the case over effectively the entire wavelength and $r(x, z, t) = r(z, t)$. For a wave with finite horizontal wavelength, λ , which is a finite multiple of the water-depth (H), the along-wave variation of $r(x, z, t)$ needs to be retained. These two properties of the horizontal structure of $r(x, z, t)$ are at the crux of the formulations outlined in the next two sections.

Inserting the density perturbation Eq. (29) into Eq. (20), a definition analogous to the free surface kinematic boundary condition (Hodges and Street, 1999) arises for the isopycnal displacement η :

$$\frac{D\eta}{Dt} = w. \quad (32)$$

When deriving the actual velocity field using the Euler-Lagrange approach, the stratified waveguide analogy is still valid, but with a time dependent stratification to account for the wave-induced changes to account for the dynamic nature of the pycnocline. The derivation is the same as previously, only replacing the fixed frame of reference by the one tracking the displaced pycnocline. The decomposition presented in Eq. (15) is still valid, as the change of frame of reference considered only involves a vertical translation in W . Therefore the vertical velocity w_{E-L} is now actually given by

$$w_{E-L}(x, z, t) = w_{Eul}(x, z - \eta, t) = -Ak \cos(kx - \omega t) W(z - \eta). \quad (33)$$

Note that in Eqs. (29) and (33) η is defined using Eq. (34) or (40), as elaborated in Secs. 3.3.1 and 3.3.2.

3.3.1 Long waves

As a first approximation, since the waves of interest are long ($\lambda/H \gg 1$) and as outlined in the previous section, the x dependence of the vertical displacement η is neglected and η is considered to depend only on the vertical position z and time t . The

displacement of the fluid in the vertical direction along the wall $\eta(x = 0, z, t)$ is therefore computed by integrating in time the
 325 w component of the velocity field. The Eulerian approach discussed previously then gives a good approximation, as a starting
 point, of the w field (Eq. (22)), and η may be derived as:

$$\eta(z, t) = \int_0^t w_E(x = 0, z, t) dt = \frac{Ak}{\omega} \sin(-\omega t) W(z). \quad (34)$$

Using the continuity equation, Eq. (21), u_{E-L} is derived accordingly. Specific attention needs to be paid to the z variation
 of the pycnocline's displacement η . In this regard, using the chain rule in differentiating $W(z - \eta)$, one obtains:

$$330 \quad \frac{\partial u_{E-L}}{\partial x} = -\frac{\partial w_{E-L}}{\partial z} = Ak \cos(kx - \omega t) \left(1 - \frac{\partial \eta}{\partial z}\right) W'(z - \eta), \quad (35)$$

leading to,

$$u_{E-L} = A \sin(kx - \omega t) \left(1 - \frac{\partial \eta}{\partial z}\right) W'(z - \eta). \quad (36)$$

An extra term depending on the z -dependence of η now appears in the expression of u_{E-L} to account for the movement of
 the pycnocline as contrasted to Eq. (23). Note also that the prime denotes a derivative with respect to the argument of W .

335 As a result, the deep-water boundary forcing functions for the Euler-Lagrange approach are defined as:

$$f_u^{E-L}(z, t) = A \sin(-\omega t) \left(1 - \frac{\partial \eta}{\partial z}\right) W'(z - \eta) \quad (37)$$

$$f_w^{E-L}(z, t) = -Ak \cos(-\omega t) W(z - \eta) \quad (38)$$

$$340 \quad f_\rho^{E-L}(z, t) = \bar{\rho}(z - \eta) - \bar{\rho}(z). \quad (39)$$

By comparing the spatial structure of the two approaches, (Fig. 3), the main difference resides in the structure of the velocity
 fields: in the Euler-Lagrange approach, the velocity field's deformation tracks that of the pycnocline's (plotted in black in
 Fig. 3 (c) and (d)), in contrast to the purely Eulerian case where the velocity field treats the pycnocline's position as constant
 (Fig. 3 (a) and (b)). Panel (e) shows how the vertical eigenfunctions computed for the wave-displaced pycnocline at the wave
 345 peak and trough are offset from the corresponding eigenfunction computed for the initial undisturbed stratification. In the
 Euler-Lagrange approach this vertical, wave-induced, pycnocline displacement is indeed accounted for. For a more detailed
 discussion of modified vertical eigenfunctions due to wave-induced displacements of the pycnocline, and a more thorough
 mathematical elaboration thereof, the interested reader is referred to the paper by Lamb (1998).

3.3.2 Waves of finite wavelength

350 So far, the dependence of η on the along wave position x has been neglected in a first approximation since the considered waves are assumed to be long. Practically, numerical simulations are often required to consider waves of finite wavelength. In this case, to accurately satisfy the continuity equation, Eq. (21), the x dependence must be accounted for and the displacement η is expressed as:

$$\eta(x, z, t) = \int_0^t w_{Eul}(x, z, t) dt = \frac{Ak}{\omega} \sin(kx - \omega t) W(z). \quad (40)$$

355 Integrating Eq. (35) now needs to take into account the x dependence of η , leading to a new expression for the horizontal velocity perturbation:

$$u_{E-L} = -\frac{\omega}{kW(z)} \left(1 - \frac{\partial \eta}{\partial z}\right) W(z - \eta) + \frac{\omega W'(z)}{kW^2(z)} \Phi(z - \eta) + B, \quad (41)$$

where Φ is the antiderivative of W and B is an integration constant. The second term in the right hand side of Eq. (41) appears to be, by evaluation of terms across the height of the domain, orders of magnitude smaller than the first one for a typically used
360 wave and is therefore dropped:

$$u_{E-L} = -\frac{\omega}{kW(z)} \left(1 - \frac{\partial \eta}{\partial z}\right) W(z - \eta) + B, \quad (42)$$

B can be derived from the fact that the horizontal velocity is zero at the depth of the pycnocline, leading to:

$$B = \frac{\omega}{kW(z_p)} \left(1 - \frac{\partial \eta}{\partial z}(0, z_p, t = 0)\right) W(z_p - \eta(0, z_p, t = 0)). \quad (43)$$

Since the right hand side of Eq. (42) is not defined on the boundaries for $z = 0$ and $z = -H$, it can be extended using a
365 continuous linear extension, finally resulting into:

$$u_{E-L}(z, t) = \begin{cases} \frac{\omega}{kW(z)} \left(1 - \frac{\partial \eta}{\partial z}\right) W(z - \eta) + B & \text{for } 0 > z > -H \\ \frac{\omega}{k} \left(1 - \frac{\partial \eta}{\partial z}(0, 0, t)\right) + B & \text{for } z = 0 \\ \frac{\omega}{k} \left(1 - \frac{\partial \eta}{\partial z}(0, -H, t)\right) + B & \text{for } z = -H \end{cases}. \quad (44)$$

This approach will hereafter be referred to as *optimized Euler-Lagrange*.

Note that, when used to implement deep-water wave-generating boundary conditions, in all final expressions for u_{E-L} , w_{E-L} and ρ'_{E-L} derived in this section or Section 3.3.1, the value of x is set to zero without any loss of generality, in a manner
370 similar to the Eulerian approach as discussed in Section 3.2.

As a result, the deep-water boundary forcing functions for the optimized Euler-Lagrange approach are defined as:

$$f_u^{optimized\ E-L}(z, t) = \begin{cases} \frac{\omega}{kW(z)} \left(1 - \frac{\partial\eta}{\partial z}\right) W(z - \eta) + B & \text{for } 0 > z > -H \\ \frac{\omega}{k} \left(1 - \frac{\partial\eta}{\partial z}(0, 0, t)\right) + B & \text{for } z = 0 \\ \frac{\omega}{k} \left(1 - \frac{\partial\eta}{\partial z}(0, -H, t)\right) + B & \text{for } z = -H \end{cases} . \quad (45)$$

$$f_w^{optimized\ E-L}(z, t) = -Ak \cos(-\omega t) W(z - \eta) \quad (46)$$

375

$$f_\rho^{optimized\ E-L}(z, t) = \bar{\rho}(z - \eta) - \bar{\rho}(z). \quad (47)$$

The associated adjustments introduced in the pressure boundary condition due to the presence of a time-dependent boundary-normal velocity field at the deep water boundary are discussed in Section 2.4.

380 Finally, per the previous discussion of Eq. (30), we emphasize that, by construction, neither of the variants of the Euler-Lagrange approach outlined are designed as exact solutions to the linearized Euler equations: perfectly shaped monochromatic waves should not be expected. As illustrated by the results in Section 3.4.3, the waves generated through the most suitable of the two Euler-Lagrange approaches (dictated by the aspect ratio λ/H at hand) are far more robust than those produced by the purely Eulerian approach. As a result, higher-amplitude longer waves can be used as forcing of fully nonlinear simulations (see Section 3.4.4).

385 3.4 Simulations of periodic internal waves in uniform-depth water

3.4.1 Numerical setup

390 Across all numerical simulations conducted in this study, the wave-based Reynolds number is held constant at $Re_w = 2.5 \times 10^5$. Such a value of Re_w is representative of laboratory scale, yet is sufficiently high to avoid any attenuation in wave amplitude in the propagation zone. The Schmidt number $Sc = \nu/\kappa$ is fixed at unity. A wave-based Froude number of $Fr = 0.2$ is linked to generated waves that may confidently be characterized as finite-amplitude and can support the development of sufficiently strong nonlinear effects as they propagate away from the forcing boundary.

395 The quasi two-layer continuous stratification profile for $\bar{\rho}(z)$, given by Eq. (3), is kept the same across all runs. A relatively thin pycnocline with $\delta/H = 0.09$ is used with a non-dimensional density jump across the pycnocline of $\Delta\rho/\rho_0 = 2N_0^2\delta/g = 1.7 \times 10^{-3}$ located at a relative position $z_p/H = -0.4$. The particular value of δ/H is chosen to mimic the thinner pycnocline of the early Fall stratification profile in a long-deep lake (Schweitzer, 2010). The deep-water-generated wave used in these simulations is chosen to have an aspect ratio $\lambda_x/H = 10.12$. Such a value of λ_x/H qualifies the wave as finite-length, albeit not short. Finally, for the particular thin-pycnocline stratification profile and choice of λ_x , the amplitude coefficient A leading

to a value of $Fr = 0.2$ corresponds to a value of $A/(\delta c) = 5$. Euler-Lagrange effects will clearly be present. The choice of λ_x/H further motivates the question as to whether the fully optimized Euler-Lagrange approach is needed.

400 All simulations are performed in a uniform-depth tank of depth H and length $L = 10\lambda_x$. The domain is chosen sufficiently long to allow the development of nonlinear effects within the generated waves. Using uniformly sized rectangular spectral elements, 224 points per wavelength λ_x , are employed in the horizontal direction, whereas 161 points span the entire water column in the vertical direction. The resolutions are given in Table 1 and the elements are uniformly spaced in both length and height. The internal grid point distribution in each element consist of non-uniformly distributed two-dimensional Gauss-
405 Lobatto-Legendre (GLL) integration points (Canuto et al., 2007).

Polynomial order p	7
Number of elements in the x -direction m_x	120
Number of elements in the z -direction m_z	20
Total number of points in the x -direction N_x	2241
Total number of points in the z -direction N_z	161
$\Delta x/H$ range	[0.0181 – 0.0656]
$\Delta z/H$ range	[0.0025 – 0.0091]

Table 1. Grid point count and resolution for the two-dimensional simulations in uniform depth tank.

3.4.2 Limitations of the Eulerian approach

The limitations of the Eulerian approach for the wave forcing are visible in a linear INSE solver (not shown here) but are more readily demonstrated in the framework of nonlinear solver of this type. As shown Fig. 4 (a), the Eulerian-generated u -velocity field, namely the shear-layer between the upper and lower lobes of opposite velocity, tracks horizontally along the location
410 of the undisturbed pycnocline (similar to the top left panel of Fig. 3) and does not follow the actual pycnocline location (see bottom left panel of Fig. 3). Immediately visible non-physical numerical features emerge near the forcing boundary at near-grid-scale, as evidenced by the lobes of alternating sign in the vertical velocity in that region. These spurious vertical velocities are a factor of two larger than the theoretically prescribed ones within the target wave leading to a commensurate reduction of the time-step by virtue of the CFL condition. Finally, non-negligible regions with density values that exceed by a factor of
415 2-to-2.5 the bounds of the background stratification are observed (see the blanked-out regions in Fig. 4 (c)). These spurious numerical effects intensify as more waves are generated for this value of $Fr = 0.2$. Further intensification of these effects is observed at $Fr = 0.5$ (not shown). In this case, the non-physical nonlinear interactions are strong enough to further amplify the near-source spurious vertical velocities and cause an aggressive, and prohibitive, reduction of the timestep .

Numerical experimentation indicates that for cases with a well-defined pycnocline the Eulerian approach produces robust
420 waves, and is effectively only valid, for small amplitude ($Fr \lesssim 0.05$, $\eta_{max}/H \lesssim 0.02$) and short wavelength waves ($\lambda/H \lesssim 5$). It is important to note that the ad hoc linearizing that leads to the Eulerian approach is effectively a linear truncation of a Taylor

series. In the amplitude tending to zero limit the Eulerian and E-L approaches match. However, even at moderate amplitudes a significant mismatch is observed (see black dotted lines in Fig. 4). Our approach retains the notation of the Eulerian approach, which is easier to implement in a software setting, but effectively implements the higher order terms in the Taylor series (at the cost of some algebra).

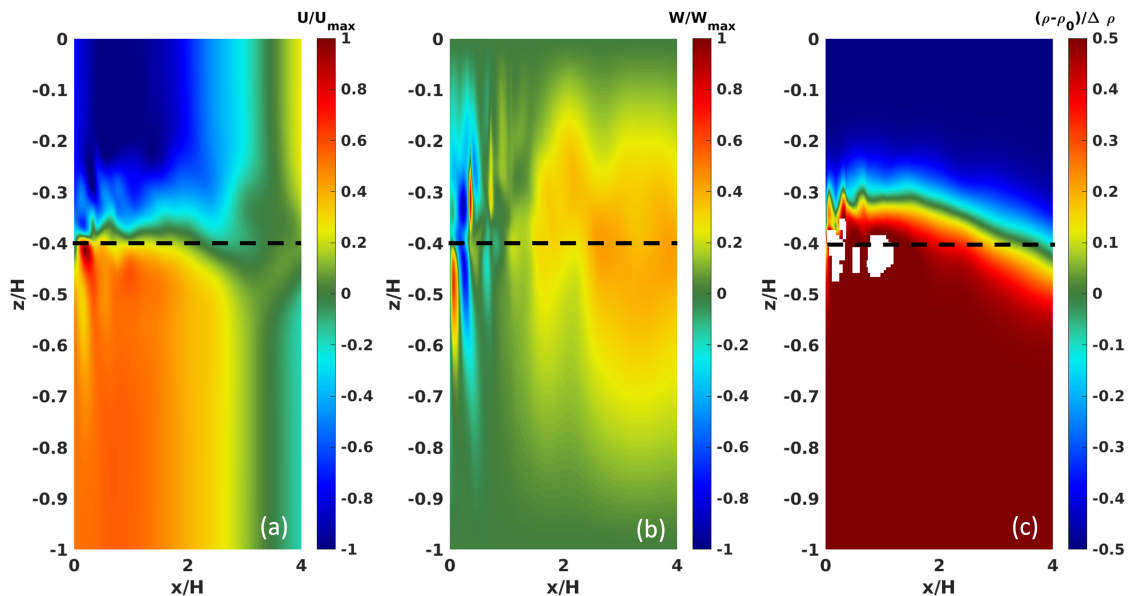


Figure 4. Fully non-linear simulation using Eulerian wave generation boundary conditions at $t/T = 5.8$ for $Fr = 0.2$ and $\lambda/H = 10$. The initial undisturbed pycnocline location is represented as a black line. Velocities (panels (a) and (b)) are normalized with their maximum values and the adjusted density (panel (c)) by the density jump at the pycnocline. Near-source near-grid-scale lobes of vertical velocity are a factor of 2-2.5 larger than that of the prescribed wave. White regions in the density contours correspond to values exceeding the colorbar limits which are set by the undisturbed background density profile.

3.4.3 Linearized Navier-Stokes simulations

To differentiate the features strictly resulting from the differences in the wave generation approach from the ones resulting from the nonlinear effects downstream of the source, the first set of simulations are restricted to solving the *linearized* incompressible Navier-Stokes equations, under the Boussinesq approximation. The nonlinear terms have been dropped in Eqs. (4), (5) and (6) analogously to what has been done in the linearized Euler equations, i.e., Eqs. (19), (20) and (21). Per the discussion of the previous section on the limitations of the Euler approach, only the Euler-Lagrange approach is considered here.

The sensitivity to including the x -dependence of the isopycnal displacement η in the Euler-Lagrange approach is assessed in Fig. 5 by examining the velocity and density fields that are produced by the approaches outlined in Sections 3.3.1 and 3.3.2 per the corresponding expressions for f_u^{E-L} and $f_u^{optimized\ E-L}$ in Eqs. (37) and (45). The forcing functions f_w and f_p have

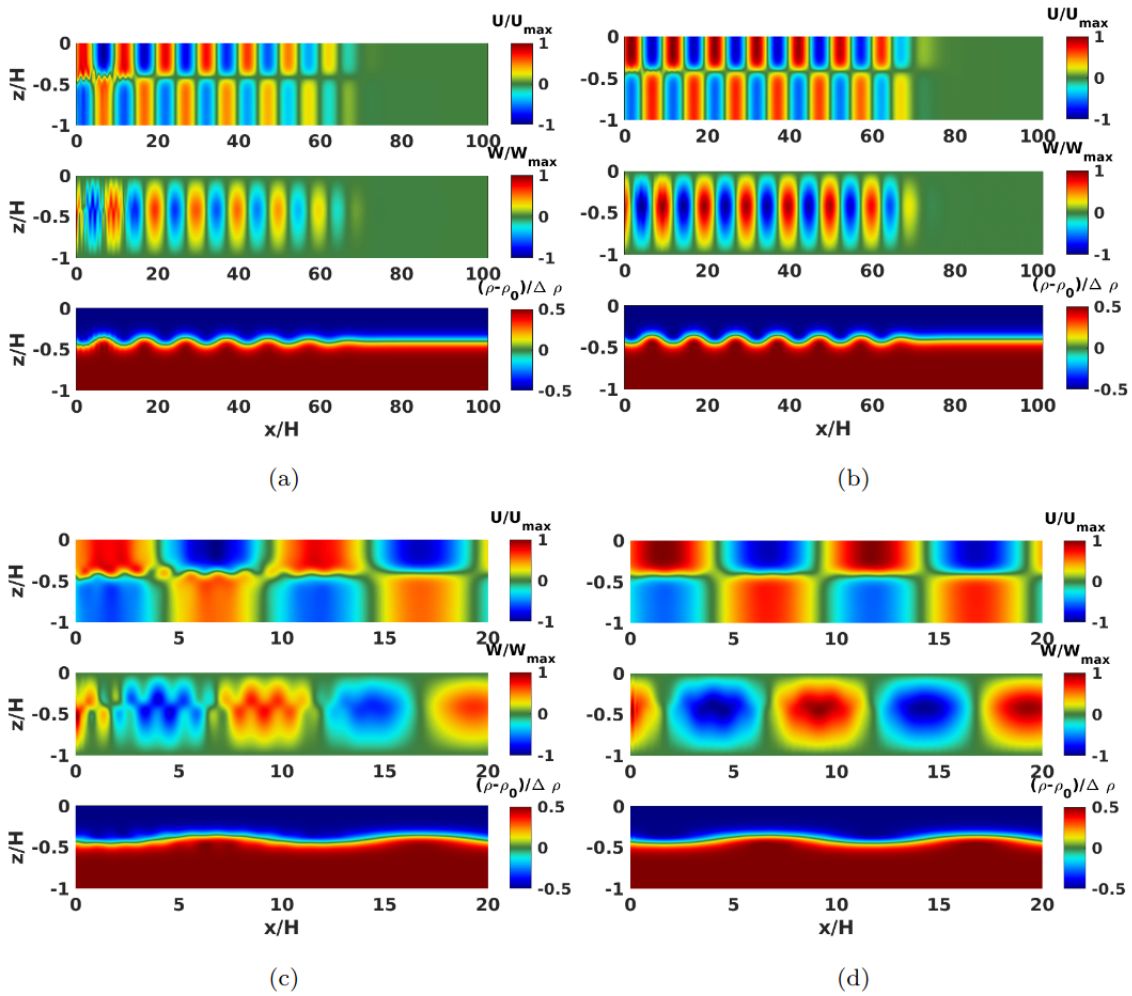


Figure 5. Comparison of the velocity and density structure generated by the two different Euler-Lagrange wave generation approaches in a fully linear simulation at $t/T = 7.4$. The left panels (a) and (c) use the Euler-Lagrange approach and the right panels (b) and (d) use the optimized one. The bottom panels (c) and (d) correspond to a zoomed view of the respective top panels (a) and (b). Velocities are normalized with their maximum values and the adjusted density by the density jump at the pycnocline.

435 the same structure in both cases and are given by Eq. (38) and Eq. (39), noting any adjustments for the x -dependence of η
in the optimized Euler-Lagrange formulation. Results are shown after approximately 7 wave periods since the initiation of
deep-water boundary wave forcing.

Close to the wave source, periodic shorter-wavelength features are observed for both approaches. These smaller-scale oscillations result from neither of the Euler-Lagrange approaches being an exact solution of the linearized Euler equations, as
440 discussed in Sec. 3.3. The amplitude and downstream persistence, however, of these shorter-wavelength effects is markedly
weaker in the optimized Euler-Lagrange approach right panels in Fig. 5, because of the finite wavelength of the generated wave

(see Sec. 3.3). To this end, the optimized Euler-Lagrange approach is the method of choice in the fully nonlinear simulations, given that our baseline wave has an aspect ratio of λ/H : using it minimizes any possible non-linear interactions between the above parasitic smaller-scale waves and the main target wave which otherwise pose non-trivial challenges for the robustness of the latter wave.

3.4.4 Fully nonlinear simulations

The resulting velocity and density fields, obtained by solving the fully nonlinear Navier Stokes Equations under the Boussinesq approximation (Eqs. (4), (5) and (6)), forced by the optimized Euler-Lagrange approach are shown in Fig. 6 after 10 wave periods. The spurious numerical features close to the boundary have been found to be significantly weaker (not shown here) as compared to what is shown in Fig. 4. Whereas the shear-layer of the horizontal velocity field tracks the oscillating pycnocline according to Fig. 3, and doesn't affect the wave generation. Additionally, no spurious mass generation is observed, with density values restricted within the limits dictated by the background stratification. Finally, near-grid-scale vertical velocity near the source remain very small in magnitude such that the wave-induced vertical velocity is the only factor controlling the timestep, as expected. The nonlinear response of the generated wave may now be examined along the propagation path without contamination by spurious nonlinear interactions due to small-scale near-source transients.

The structure of the generated waves is indeed visibly modified by nonlinearity as they propagate away from their source, with different waveform geometries becoming immediately identifiable as a function of distance from the source. Fig. 7 attempts to offer such a waveform classification across three different sub-windows along the propagation path. Fig. 7(a) shows waves of depression that develop close to the source. Since the particular waves have large flat plateaus and narrow troughs, a clear similarity with cnoidal waves (Boyd, 2015) is suggested. During a transitional phase, shown in Fig. 7(c), the wave troughs broaden. Further downstream the waves tend to assume a near-sinusoidal shape with peaks and troughs of comparable width (Fig. 7(e)).

A more quantitative description of the different types of observed waveforms is enabled by examining the corresponding along-wave spectral content. One-dimensional spatial fast Fourier transforms (FFT) of the density are computed for each sub window, focused at the depth of the undisturbed pycnocline, which in one-dimensional streamwise Fourier spectra of the density $\hat{\rho}(k)$. Special attention needs to be paid when computing the FFTs for the simulations at hand, since the internal grid point distribution within each spectral is non-uniform (Section 3.4.1). A non-uniform FFT algorithm is therefore used (Dutt and Rokhlin, 1993; Potter et al., 2017), as it is well tested and readily available.

Closer examination of the right column of panels in Fig. 7, suggests that the along-wave spectral content has power spectral density in regions not specified by the forcing. In particular, a strong second harmonic persists at a downstream distance as large as $60H$. Further downstream from the forcing boundary, the amplitude of this harmonic significantly attenuates resulting in a wave that is closer to being monochromatic (as confirmed by the visualization of Fig. 7 (e)). In the context of a fully non-linear simulation with a sloping boundary, adjusting the length of the section of the computational domain over which the waves propagate prior to reaching the slope allows one to decide how much waves are allowed to naturally adjust due to their finite amplitude and dispersion. Equivalent simulations, which separate slope from source by only a fraction of the horizontal

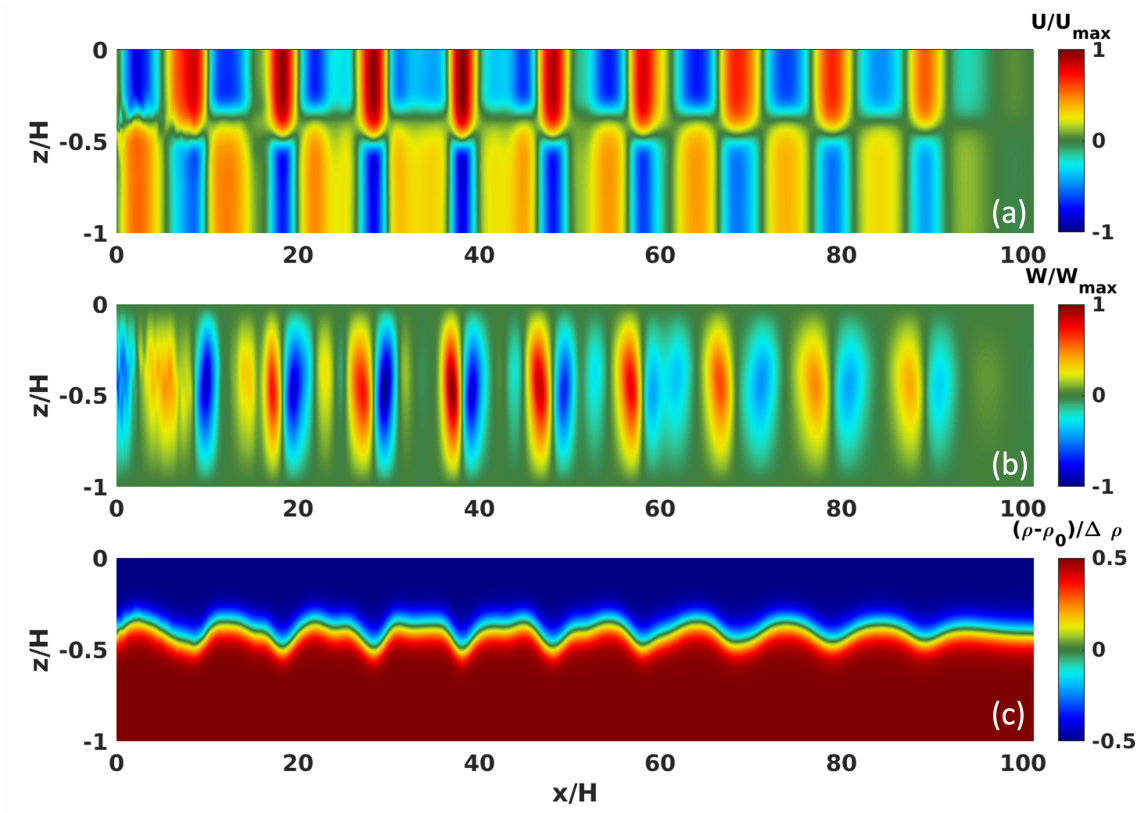


Figure 6. Fully non-linear simulation using optimized Euler-Lagrange wave generation boundary conditions at $t/T = 10$. Velocities (panels (a) and (b)) are normalized with their maximum values and the adjusted density (panel (c)) by the density jump at the pycnocline.

wavelength (Masunaga et al., 2015, 2016), are not expected to support a nonlinearly adjusted (and potentially steepened) waveform as the incident wave reaches a slope.

The vertically integrated kinetic energy (KE), at any down-stream position x , is:

$$KE = \int_{-H}^0 \frac{1}{2} \rho_0 (u^2 + w^2) dz. \quad (48)$$

480 KE is shown as a function of time and position for both the fully linear case Fig. 8 (a) and non-linear case Fig. 8 (b). The theoretically prescribed characteristic of energy transport given by the wave speed $c = \lambda_x/T$ is also plotted. Fig. 9 presents the interpolation of the kinetic along the prescribed characteristic of energy transport in the linear case shown in white in Fig. 8 (a). The slope of the KE contours, a measure of the group velocity, appears to match well with the theoretical value. Viscous decay can be considered negligible since the wave-based Reynolds number is chosen $Re_w = (\lambda_x^2/\nu)/T \gg 1$. The deviation
 485 along the characteristic in Fig. 9 can therefore be attributed to the dispersive aspect of the continuous two-layer stratification.

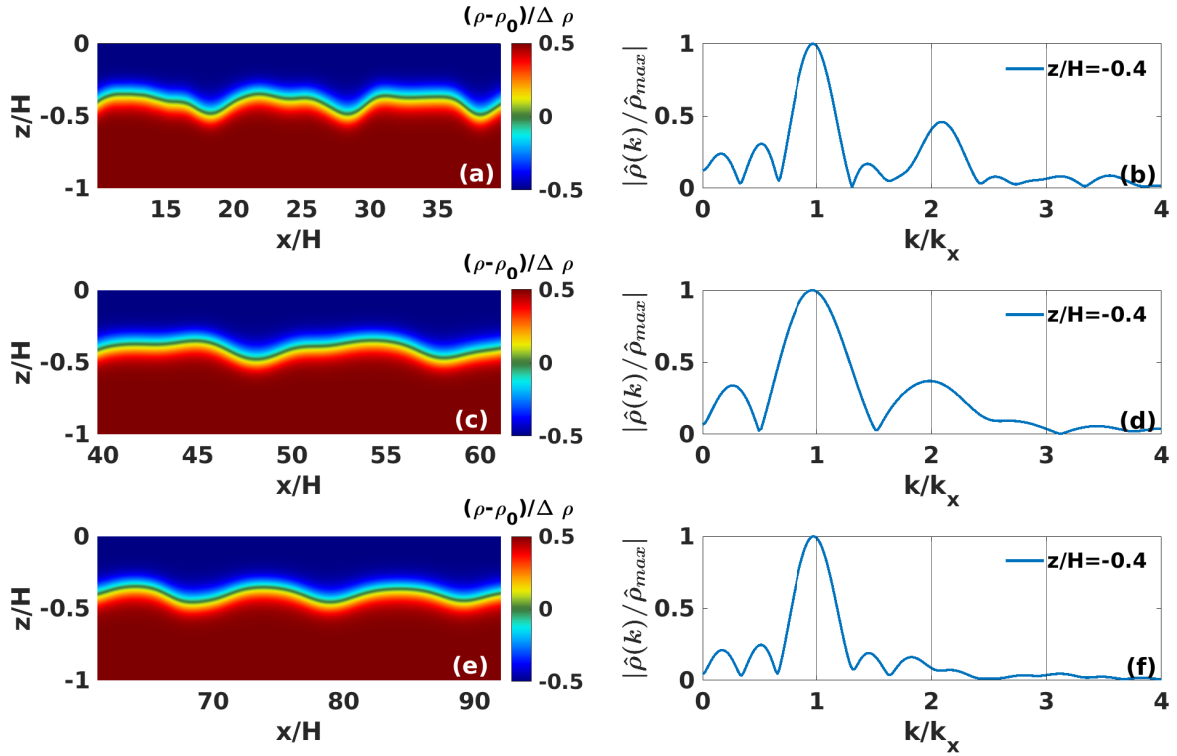


Figure 7. Exploded view of full density contours at different downstream locations for the waves shown in Fig. 6 illustrating the development of wave forms (panels (a), (c) and (e)). Respective streamwise Fourier spectra $\hat{\rho}$ of $\rho(x)$ computed at $z/H = z_p = -0.4$ and $t/T = 10$ normalized by the maximum peak depending on the wavenumber normalized by the prescribed wave number k_x (panels (b), (d) and (f)).

In the non-linear case, characteristics also appear to be parallel to the theoretical solution, even if the KE is not constant along it due to non-linearities generating extra wavelengths.

4 Discussion

The generation process of finite-amplitude periodic waves through time-dependent deep-water Dirichlet boundary condition has been examined for the case of a quasi two-layer continuous stratification (Fig. 1). In the case of a linear stratification, N^2 is constant in time and space and therefore Eq. (16) has an analytical solution W_n . Such a solution leads to an exact expression of the perturbation fields for the linear Euler equations under the Boussinesq approximation with an analytical vertical structure, with an explicit time dependence (see Appendix B). The amplitude of the generated waves can non-trivially exceed the limit prescribed by linear theory without any impact on wave robustness as evidenced by the deep-water waves used in the linearly stratified simulations of Winters (Winters, 2015).

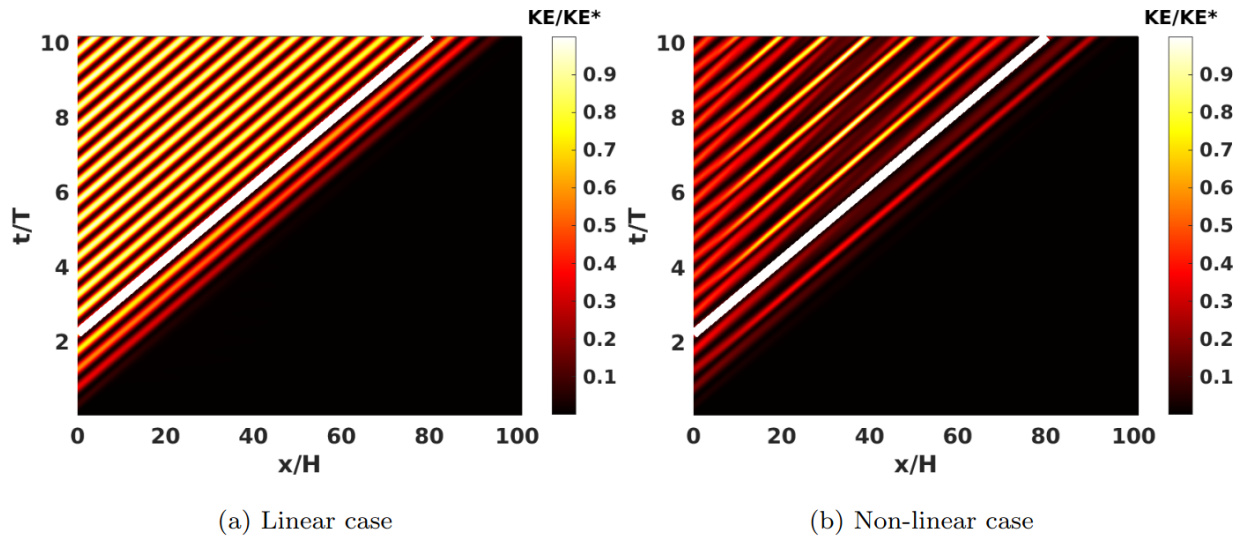


Figure 8. Vertically integrated kinetic energy KE normalized by its maximum value KE^* as a function of the downstream position and time for both the linear and non-linear case. The white line corresponds the theoretical energy transport characteristic $x = c \times t$.

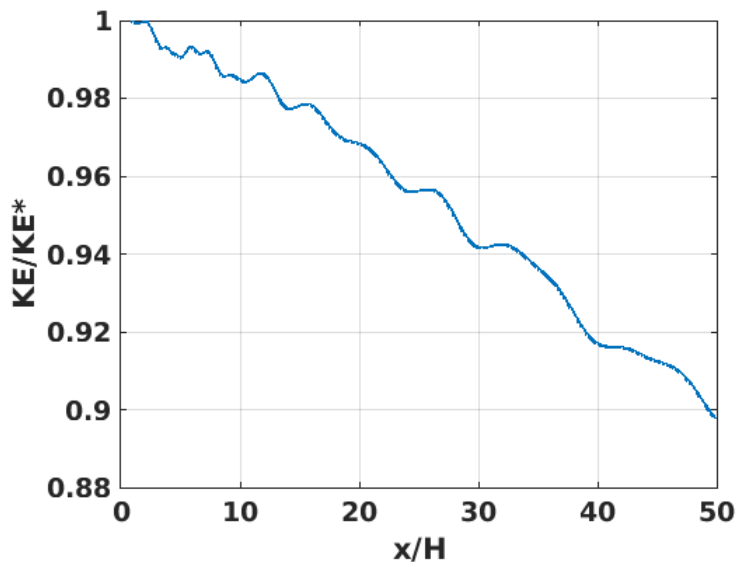


Figure 9. Kinetic energy along the prescribed characteristic of energy transport in the linear case shown in Fig. 8 (a).

As described in Section 3, the quasi-two-layer stratification studied here appears to be more complex. In this context we don't have an analytical expression for $W(z, t)$, leading to the different approximations introduced in this study. These extra layers of approximations will therefore tighten the amplitude limitations of the wave that can be generated. Nevertheless depending

on the chosen stratification, numerical experiments (not shown here) have demonstrated that robust waves up to $Fr = 0.5$ are
500 achievable using the optimized Euler-Lagrange approach.

Another important feature that has been demonstrated by Fig. 7, is the fact that in the quasi two-layer continuous stratification
the forcing produces wave-trains that are non-monochromatic. Eq. (44) reveals that the optimized Euler-Lagrange approach
results from the multiplication of temporary-oscillating terms, leading to the appearance of multiple harmonic wavelengths in
the generated wave. Sufficiently downstream of the source, the strength of these harmonics seems to diminish for the $Fr = 0.2$
505 waves shown in Fig. 7(v), with wave-induced perturbations that may be regarded as assuming a near-sinusoidal waveform.
Nonetheless, the wave-trains at the same downstream location in our experiments with $Fr = 0.5$ (not shown here) are found to
remain remarkably nonlinear with extremely steep fronts therein.

Per the literature review in the introduction, the only other computational study considering the generation of long finite-
amplitude waves in a two-layer stratification, with sufficient distance for the waves to develop downstream from the source,
510 that the authors are aware is that of Dauhajre et al. (2021). We suspect that no issues were reported in regards to the deep-water
generated waves for two reasons. First, motivated by apparently different objectives than this study, the use of wave aspect ratio
of $\lambda/H = 200$ is remarkably long and, most likely, restrictive if a turbulence-resolving capability (and not a turbulence parame-
terization) is preferred. Additionally, the inferred normalized pycnocline thickness value of $\delta/H = 0.35$ is more representative
of that in the oceanic continental shelf and not of a deep and long seasonally stratified lake, the primary motivator of this study.
515 Most importantly, noting that $Ak = W_{max}$, where W_{max} is the maximum wave-induced vertical velocity, Dauhajre et al. work
with a typical value of $A/(\delta c) \approx 1.8$. These non-dimensional parameter values along with any reduction of curvature at the
base of the pycnocline through the insertion of a weakly, yet non-trivially, stratified lower layer may diminish the intensity
of any Euler-Lagrange effects per Eq. (30) and the associated discussion. Finally, it is unclear how the numerical dissipation
built into the K-Profile-Parameterization (Large et al., 1994) actively used by Dauhajre et al. (2021) may have damped out any
520 near-source short-wavelength initialization transients such as those reported in Section 3.4.3.

5 Conclusions

This study has examined the formulation of robust finite amplitude periodic internal-wave generating boundary conditions
for a nonlinear stratification, highlighting extra levels of subtlety compared to the linear stratification case, while relying on
a higher-order accuracy spectral element method to discretize the governing equations. The commonly used Eulerian ap-
525 proach, which relies on a fixed reference frame, is found to develop non-trivial errors when implemented in simulations with
a sharp quasi-two-layer continuous stratification and higher-amplitude internal waves with a horizontal-wavelength-to-depth
(wave aspect) ratio that is finite, albeit not excessively large. The errors result because the prescribed wave forcing assumes a
fixed/unperturbed pycnocline and does not account for the upstream and vertical wave-induced displacement of the pycnocline.
This mismatch between fixed wave-forcing and moving pycnocline is shown to scale with the parameter $A/(\delta c)$, where A is
530 a measure of wave amplitude, δ is the pycnocline thickness and c is the wave propagation speed. Simulations with values of
 $A/(\delta c) = 5$ show spurious mass generation near the wave-generating source with accompanying unphysical near-grid-scale

vertical velocities that can detrimentally reduce the computational timestep, and even prohibitively restrict it for a long enough time and higher values of wave-induced Froude number, Fr . The minimal numerical dissipation of the spectral element method can not damp these spurious numerical features.

535 For values of $A/(\delta c)$ sufficiently larger than unity, an Euler-Lagrange approach needs to be used instead, which does account for the above pycnocline displacement, in the wave generation. Although an exact solution of the linearized Euler equations under the Boussinesq approximation is not actually attained through this approach, the resulting waves are sufficiently robust: they can propagate away from the source ; nonlinear adjustments of their waveform is possible through leveraging the higher-order-accuracy spectral element scheme.

540 The findings of this study will serve as a platform to enable a detailed numerical study of internal swash zones (ISZ), zones driven by the interaction of long periodic nonlinear internal waves with a sloping boundary. Such simulations will aim to investigate the parameter space in two-dimensions which would include wave Froude number, pycnocline thickness and depth, wave-aspect-ratio, slope value and the role of no-slip vs. free-slip boundary conditions, particularly on the slope. Select two-dimensional studies will operate as the springboard for full-scale three-dimensional turbulence-resolving simulations These
545 larger simulations may invariably be restricted by existing computational resources to wave aspect ratios in the range [20, 40]. As our interests are motivated by internal swash zones in seasonally stratified deep lakes lakes, we will use a two-layer continuous stratification with thinner pycnoclines typical of such environments (Schweitzer, 2015). As such, the parameter $A/(\delta c)$ will be non-trivially larger than unity. To address this region of parameter space, an Euler-Lagrange approach is needed to account for the wave-induced displacement of the isopycnal field in both vertical and horizontal directions. The optimized
550 Euler-Lagrange approach will be used to generate robust high-amplitude deep-water internal waves, at values of Froude number up to $Fr = 0.2$.

A parallel avenue of future investigation of the findings of this paper may be their translation to experimental internal wave generators. Horizontally oscillating paddles are reported as limited to significantly short waves with aspect ratio around 10 (Ghassemi et al., 2022). The vertically-stacked-plate/eccentric-camshaft structure of Mercier, Gostiaux and co-workers
555 (Mercier et al., 2010; Gostiaux et al., 2006), through its ability to reproduce a baroclinic structure in the vertical, may be the most amenable experimental technique to adopting aspects of the optimized Euler-Lagrange approach presented here.

Appendix A: Spectral Element Method

Following the work of Diamantopoulos et al. (2022), the Poisson problem (see Eq. (14)) can be rewritten as:

$$-\nabla_{xz}^2 p(x, z) = f, \quad (\text{A1})$$

560 The discretization of the laplacian in the non-homogeneous directions x - z is presented. Let $\mathcal{V}^N \subset H^1(\Omega)$, be a finite subspace where $p, v \in \mathcal{V}^N$ are a part of the solution. Accordingly, the weak form of Eq. (A1) under the Galerkin approximation becomes

$$\int_{\Omega} \nabla v \cdot \nabla p d\Omega = \int_{\Omega} v f d\Omega + \oint_{\partial\Omega} v \nabla p \cdot \mathbf{n} dS, \quad (\text{A2})$$

where $\nabla p \cdot \mathbf{n} = \partial p / \partial \mathbf{n}$ is the natural boundary condition (Deville et al., 2002). By defining \mathcal{V}^N as the finite subspace spanned by two-dimensional Lagrangian basis functions up to order N , $\mathcal{V}^N = \text{span}\{h_1(x, z), \dots, h_n(x, z)\}$, p and v are approximated as $p = \sum_k p_k h_k$ and $v = \sum_k v_k h_k$ where $k \in \{1, \dots, n\}$ is the corresponding index set, and n is the total number of degrees of freedom in the x - z plane. Note that each element has the same polynomial order. Thus, the discretized Eq (A2) is written in a matrix form

$$K\mathbf{p} = M\mathbf{f} \Rightarrow K\mathbf{p} = \mathbf{g}, \quad (\text{A3})$$

where $K_{ij} = \int_{\Omega} \nabla h_i \cdot \nabla h_j d\Omega$ and $M_{ij} = \int_{\Omega} h_i h_j d\Omega$ are the respective entries of the assembled stiffness and mass matrices (Deville et al., 2002) where $i, j \in \{1, \dots, n\}$. Note that the viscous/diffusive equations for the velocity and density field follow the same weak-form-based formulation and discretization.

A non-overlapping, domain decomposition (DD) method with iterative substructuring/static condensation is when solving for the pressure (Karniadakis and Sherwin, 2013). In tandem with a logically Cartesian topology, Eq. (A3) is broken down into a hierarchy of smaller problems with homogeneous Dirichlet boundary conditions for the two levels of the condensation (Karniadakis and Sherwin, 2013; Huisman et al., 2017; Deville et al., 2002). Once the second and last stage of the DD is reached, a Schur complement problem on the vertical interfaces, Γ^v , of the subdomains is iteratively solved. In the context of hierarchy of problems, a subsequent backwards sweep ensures the solution on the global computational domain.

A simple strategy is adopted for the numerical solution of the viscous and diffusive parts of the solver. It is during this step of the solver where boundary conditions for the velocity field and the density perturbation are enforced (Diamantopoulos et al., 2021). Following the discretization presented above, the respective Helmholtz matrix \mathbf{H}^u is given by

$$\mathbf{H}^u = \alpha \mathbf{K} + \mathbf{M}, \quad (\text{A4})$$

where the time-step coefficient α scales linearly with $\nu \Delta t$ or $\kappa \Delta t$.

Appendix B: Details on the derivation of the vertical structure in the linear stratification case

In the case of a linear stratification, we have by definition:

$$N(z) = N_0 \quad (\text{B1})$$

Eq. (16) becomes a classic second order linear differential equation, analogous to that of a simple harmonic oscillator. The solution is oscillatory in z :

$$W_n(z) = \sin\left(\frac{n\pi z}{H}\right) \text{ with } k_n = \frac{n\pi}{H} \left(\frac{\omega^2}{N^2 - \omega^2}\right)^{1/2} \quad (\text{B2})$$

590 **Appendix C: Subtleties of the implementation of the time-dependent deep-water boundary conditions**

To implement the different time-dependent deep-water boundary conditions approaches described in Sections 3.2 and 3.3, the eigenfunction $W(z)$ and corresponding eigenvalue k need to be calculated from Eqs. (16) and (17). A high-order spectral element method (Diamantopoulos et al., 2022) is used to for this purpose.

The values of the eigenfunction, and its vertical derivative, on locations offset from the actual grid points, $W(z - \eta)$ and
595 $W'(z - \eta)$ are required in either of the Euler-Lagrange approaches (see Section 3.3). These values are obtained at each time step through a cubic spline interpolation in the vertical.

Additionally, to reduce transient-driven contamination of the generated deep-water waves and force both velocity components and density perturbation to be zero at the deep-water boundary at time $t = 0$, the amplitude of the boundary forcing is ramped up in time through application of an exponential envelope. The three forcing expressions for u , w and ρ' (see Sections
600 3.2 and 3.3) are multiplied by an envelope function, $f(t)$, defined by:

$$f(t) = \left(1 - \exp\left(-\frac{t}{\tau}\right) \right) \quad (\text{C1})$$

where τ is a characteristic time scale of the ramp-up constrained by $\tau \ll T$ and set to $\tau = \frac{5}{100}T$ in this study

Code and data availability. All simulation output and data analysis scripts are publicly available on a dedicated Globus Online File Server, constructed in collaboration with Cornell's Center for Advanced Computing, as mandated by the research grant Data Management Plan
605 submitted to the U.S. National Science Foundation. The web access link is <https://diamessis.github.io/>. The path to the data storage directory is *CAC Archive 2/DTN/pjd38_0002* (subdirectory name: "Diamessis Euler Lagrange Periodic IWs") on Cornell's Center for Advanced Computing archival system.

Author contributions. **Pierre Lloret:** Conceptualization, Data curation, Investigation, Methodology, Software, Visualization, Writing - original draft. **Peter J. Diamessis:** Conceptualization, Funding acquisition, Project administration, Resources, Supervision, Writing - original
610 draft. **Marek Stastna:** Conceptualization, Writing - original draft. **Greg N. Thomsen:** Software, Writing - review & editing.

Competing interests. The authors declare that they have no conflict of interest.

Acknowledgements. Financial support is gratefully acknowledged from National Science Foundation - Division of Ocean Sciences (OCE) Grant 1948251. This work used Anvil2 at Rosen Center for Advanced Computing through allocation EES200010 from the Advanced Cyber-infrastructure Coordination Ecosystem: Services & Support (ACCESS) program, which is supported by National Science Foundation grants

615 #2138259, #2138286, #2138307, #2137603, and #2138296. Discussions on generation and breaking of internal waves in internal swash zones with Profs. Edwin (Todd) Cowen and Erika McPhee Shaw and Dr. Seth Schweitzer are gratefully acknowledged.

References

- Boegman, L.: Currents in Stratified Water Bodies 2: Internal Waves, in: Encyclopedia of Inland Waters, edited by Likens, G. E., pp. 539–558, Academic Press, Oxford, 2009.
- 620 Boegman, L. and Ivey, G. N.: Flow separation and resuspension beneath shoaling nonlinear internal waves, *Journal of Geophysical Research: Oceans*, 114, 2009.
- Boegman, L. and Stastna, M.: Sediment resuspension and transport by internal solitary waves, *Annual review of fluid mechanics*, 51, 129–154, 2019.
- Boegman, L., Ivey, G., and Imberger, J.: The energetics of large-scale internal wave degeneration in lakes, *Journal of Fluid Mechanics*, 531, 625 159 – 180, <https://doi.org/10.1017/S0022112005003915>, 2005.
- Boyd, J.: Dynamical Meteorology | Solitary Waves, in: Encyclopedia of Atmospheric Sciences (Second Edition), edited by North, G. R., Pyle, J., and Zhang, F., pp. 417–422, Academic Press, Oxford, second edition edn., <https://doi.org/10.1016/B978-0-12-382225-3.00374-1>, 2015.
- Canuto, C., Hussaini, M., Quarteroni, A., and Zang, T.: Spectral Methods: Evolution to Complex Geometries and Applications to Fluid Dynamics, Scientific Computation, Springer Berlin Heidelberg, 2007.
- 630 Cheriton, O. M., Storlazzi, C. D., and Rosenberger, K. J.: Observations of wave transformation over a fringing coral reef and the importance of low-frequency waves and offshore water levels to runup, overwash, and coastal flooding, *Journal of Geophysical Research: Oceans*, 121, 3121–3140, <https://doi.org/10.1002/2015JC011231>, 2016.
- Cowen, E. A., Sou, I. M., Liu, P. L.-F., and Raubenheimer, B.: Particle Image Velocimetry Measurements within a Laboratory-Generated Swash Zone, *Journal of Engineering Mechanics*, 129, 1119–1129, [https://doi.org/10.1061/\(ASCE\)0733-9399\(2003\)129:10\(1119\)](https://doi.org/10.1061/(ASCE)0733-9399(2003)129:10(1119)), 2003.
- 635 Dauhajre, D. P., Molemaker, M. J., McWilliams, J. C., and Hypolite, D.: Effects of Stratification on Shoaling Internal Tidal Bores, *Journal of Physical Oceanography*, 51, 3183 – 3202, <https://doi.org/10.1175/JPO-D-21-0107.1>, 2021.
- Deville, M. O., Fischer, P. F., Mund, E., et al.: High-order methods for incompressible fluid flow, vol. 9, Cambridge university press, 2002.
- Diamantopoulos, T., Diamessis, P. J., and Stastna, M.: On the formulation and implementation of the stress-free boundary condition over deformed bathymetry using a spectral-element-method-based incompressible Navier–Stokes equations solver, *Ocean Modelling*, 165, 640 101 834, <https://doi.org/10.1016/j.ocemod.2021.101834>, 2021.
- Diamantopoulos, T., Joshi, S. M., Thomsen, G. N., Rivera-Rosario, G., Diamessis, P. J., and Rowe, K. L.: A high accuracy/resolution spectral element/Fourier–Galerkin method for the simulation of shoaling non-linear internal waves and turbulence in long domains with variable bathymetry, *Ocean Modelling*, 176, 102 065, <https://doi.org/10.1016/j.ocemod.2022.102065>, 2022.
- 645 Dunphy, M., Subich, C., and Stastna, M.: Spectral methods for internal waves: indistinguishable density profiles and double-humped solitary waves, *Nonlinear Processes in Geophysics*, 18, 351–358, <https://doi.org/10.5194/npg-18-351-2011>, 2011.
- Dutt, A. and Rokhlin, V.: Fast Fourier Transforms for Nonequispaced Data, *SIAM Journal on Scientific Computing*, 14, 1368–1393, <https://doi.org/10.1137/0914081>, 1993.
- Elfrink, B. and Baldock, T.: Hydrodynamics and sediment transport in the swash zone: a review and perspectives, *Coastal Engineering*, 45, 650 149–167, [https://doi.org/10.1016/S0378-3839\(02\)00032-7](https://doi.org/10.1016/S0378-3839(02)00032-7), 2002.
- Emery, K. O. and Gunnerson, C. G.: Internal Swash and Surf, *Proceedings of the National Academy of Science*, 70, 2379–2380, <https://doi.org/10.1073/pnas.70.8.2379>, 1973.

- Gear, J. A. and Grimshaw, R.: A second-order theory for solitary waves in shallow fluids, *The Physics of Fluids*, 26, 14–29, <https://doi.org/10.1063/1.863994>, 1983.
- 655 Gerkema, T. and Zimmerman, J.: An introduction to internal waves, *Lecture Notes*, Royal NIOZ, Texel, 207, 2008.
- Ghassemi, A., Zahedi, S., and Boegman, L.: Bolus formation from fission of nonlinear internal waves over a mild slope, *Journal of Fluid Mechanics*, 932, A50, <https://doi.org/10.1017/jfm.2021.1033>, 2022.
- Gostiaux, L., Didelle, H., Mercier, S., and Dauxois, T.: A novel internal waves generator, *Experiments in Fluids*, 42, <https://doi.org/10.1007/s00348-006-0225-7>, 2006.
- 660 Grace, A., Stastna, M., and Poulin, F. J.: Numerical simulations of the shear instability and subsequent degeneration of basin scale internal standing waves, *Phys. Rev. Fluids*, 4, 014 802, <https://doi.org/10.1103/PhysRevFluids.4.014802>, 2019.
- Hodges, B. R. and Street, R. L.: On Simulation of Turbulent Nonlinear Free-Surface Flows, *Journal of Computational Physics*, 151, 425–457, <https://doi.org/10.1006/jcph.1998.6166>, 1999.
- Hosegood, P., Bonnin, J., and van Haren, H.: Solibore-induced sediment resuspension in the Faeroe-Shetland Channel, *Geophysical Research Letters*, 31, <https://doi.org/10.1029/2004GL019544>, 2004.
- 665 Huismann, I., Stiller, J., and Fröhlich, J.: Factorizing the factorization—a spectral-element solver for elliptic equations with linear operation count, *Journal of Computational Physics*, 346, 437–448, 2017.
- Karniadakis, G. and Sherwin, S.: *Spectral/hp element methods for computational fluid dynamics*, Oxford University Press, 2013.
- Karniadakis, G. E., Israeli, M., and Orszag, S. A.: High-order splitting methods for the incompressible Navier-Stokes equations, *Journal of Computational Physics*, 97, 414–443, 1991.
- 670 Kundu, P. K., Cohen, I. M., and Dowling, D.: *Fluid Mechanics 4th edition*, 2008.
- Lamb, K. G.: *Theoretical Descriptions of Shallow-Water Solitary Internal Waves: Comparisons with Fully Nonlinear Internal Waves*, Presented at the WHOI/IOS/ONR Internal Solitary Wave Workshop, Woods Hole Oceanographic Institution, 1998.
- Lamb, K. G. and Yan, L.: The evolution of internal wave undular bores: comparisons of a fully nonlinear numerical model with weakly nonlinear theory, *Journal of physical oceanography*, 26, 2712–2734, 1996.
- 675 Large, W. G., McWilliams, J. C., and Doney, S. C.: Oceanic vertical mixing: A review and a model with a nonlocal boundary layer parameterization, *Reviews of Geophysics*, 32, 363–403, <https://doi.org/10.1029/94RG01872>, 1994.
- Lemckert, C. and Imberger, J.: *Turbulent Benthic Boundary Layer Mixing Events in Fresh Water Lakes*, chap. 35, pp. 503–516, American Geophysical Union (AGU), ISBN 9781118665381, <https://doi.org/10.1029/CE054p0503>, 1998.
- 680 Lucas, A. J. and Pinkel, R.: Observations of Coherent Transverse Wakes in Shoaling Nonlinear Internal Waves, *Journal of Physical Oceanography*, 52, 1277 – 1293, <https://doi.org/10.1175/JPO-D-21-0059.1>, 2022.
- Martini, K. I., Alford, M. H., Kunze, E., Kelly, S. M., and Nash, J. D.: Internal Bores and Breaking Internal Tides on the Oregon Continental Slope, *Journal of Physical Oceanography*, 43, 120 – 139, <https://doi.org/10.1175/JPO-D-12-030.1>, 2013.
- Masunaga, E., Homma, H., Yamazaki, H., Fringer, O. B., Nagai, T., Kitade, Y., and Okayasu, A.: Mixing and sediment resuspension associated with internal bores in a shallow bay, *Continental Shelf Research*, 110, 85–99, <https://doi.org/10.1016/j.csr.2015.09.022>, 2015.
- 685 Masunaga, E., Fringer, O. B., Yamazaki, H., and Amakasu, K.: Strong turbulent mixing induced by internal bores interacting with internal tide-driven vertically sheared flow, *Geophysical Research Letters*, 43, 2094–2101, <https://doi.org/10.1002/2016GL067812>, 2016.
- McPhee-Shaw, E.: Boundary–interior exchange: Reviewing the idea that internal-wave mixing enhances lateral dispersal near continental margins, *Deep Sea Research Part II: Topical Studies in Oceanography*, 53, 42–59, <https://doi.org/10.1016/j.dsr2.2005.10.018>, 2006.

- 690 McPhee-Shaw, E. E. and Kunze, E.: Boundary layer intrusions from a sloping bottom: A mechanism for generating intermediate nepheloid layers, *Journal of Geophysical Research (Oceans)*, 107, 3050, <https://doi.org/10.1029/2001JC000801>, 2002.
- Mercier, M. J., Martinand, D., Mathur, M., Gostiaux, L., Peacock, T., and Dauxois, T.: New wave generation, *Journal of Fluid Mechanics*, 657, 308–334, <https://doi.org/10.1017/S0022112010002454>, 2010.
- Mercier, M. J., Gostiaux, L., Helfrich, K., Sommeria, J., Viboud, S., Didelle, H., Ghaemsaidi, S. J., Dauxois, T., and Peacock, T.: Large-
695 scale, realistic laboratory modeling of M2 internal tide generation at the Luzon Strait, *Geophysical Research Letters*, 40, 5704–5709, <https://doi.org/10.1002/2013GL058064>, 2013.
- Moore, C. D., Koseff, J. R., and Hult, E. L.: Characteristics of bolus formation and propagation from breaking internal waves on shelf slopes, *Journal of Fluid Mechanics*, 791, 260–283, <https://doi.org/10.1017/jfm.2016.58>, 2016.
- Nakayama, K. and Imberger, J.: Residual circulation due to internal waves shoaling on a slope, *Limnology and Oceanography*, 55, 1009–
700 1023, <https://doi.org/10.4319/lo.2010.55.3.1009>, 2010.
- Nash, J. D., Kunze, E., Toole, J. M., and Schmitt, R. W.: Internal Tide Reflection and Turbulent Mixing on the Continental Slope, *Journal of Physical Oceanography*, 34, 1117, [https://doi.org/10.1175/1520-0485\(2004\)034<1117:ITRATM>2.0.CO;2](https://doi.org/10.1175/1520-0485(2004)034<1117:ITRATM>2.0.CO;2), 2004.
- Omand, M. M., D’Asaro, E. A., Lee, C. M., Perry, M. J., Briggs, N., Cetinić, I., and Mahadevan, A.: Eddy-driven subduction exports particulate organic carbon from the spring bloom, *Science*, 348, 222–225, <https://doi.org/10.1126/science.1260062>, 2015.
- 705 Potter, S. F., Gumerov, N. A., and Duraiswami, R.: Fast interpolation of bandlimited functions, in: 2017 IEEE International Conference on Acoustics, Speech and Signal Processing (ICASSP), pp. 4516–4520, <https://doi.org/10.1109/ICASSP.2017.7953011>, 2017.
- Rogers, J. S., Rayson, M. D., Ko, D. S., Winters, K. B., and Fringer, O. B.: A framework for seamless one-way nesting of internal wave-resolving ocean models, *Ocean Modelling*, 143, 101–146, <https://doi.org/10.1016/j.ocemod.2019.101462>, 2019.
- Schweitzer, S.: The Effects Of Runoff And Upwelling Events On The Water Quality Of The Southern Shelf Of Cayuga Lake, Master’s thesis, Cornell University, 2010.
710
- Schweitzer, S.: Physical Processes In A Long Narrow Deep Lake, Ph.D. thesis, Cornell University, 2015.
- Stastna, M.: *Internal Waves in the Ocean: Theory and Practice*, vol. 9, Springer Nature, 2022.
- Stevens, C. L., Abraham, E. R., Moore, C. M., Boyd, P. W., and Sharples, J.: Observations of Small-Scale Processes Associated with the Internal Tide Encountering an Island, *Journal of Physical Oceanography*, 35, 1553 – 1567, <https://doi.org/10.1175/JPO2754.1>, 2005.
- 715 Taylor, J. R.: Turbulence and mixing in the boundary layer generated by shoaling internal waves, *Dynamics of Atmospheres and Oceans*, 19, 233–258, [https://doi.org/10.1016/0377-0265\(93\)90038-9](https://doi.org/10.1016/0377-0265(93)90038-9), 1993.
- Thorpe, S.: Some dynamical effects of internal waves and the sloping sides of lakes, *Coastal and Estuarine Studies*, pp. 441–460, 1998.
- Thorpe, S. A., Keen, J. M., Jiang, R., and Lemmin, U.: High-Frequency Internal Waves in Lake Geneva, *Philosophical Transactions: Mathematical, Physical and Engineering Sciences*, 354, 237–257, 1996.
- 720 Ting, F. C. and Kirby, J. T.: Dynamics of surf-zone turbulence in a spilling breaker, *Coastal Engineering*, 27, 131–160, [https://doi.org/10.1016/0378-3839\(95\)00037-2](https://doi.org/10.1016/0378-3839(95)00037-2), 1996.
- Turkington, B., Eydeland, A., and Wang, S.: A Computational Method for Solitary Internal Waves in a Continuously Stratified Fluid, *Studies in Applied Mathematics*, 85, 93–127, <https://doi.org/10.1002/sapm199185293>, 1991.
- Wallace, B. C. and Wilkinson, D. L.: Run-up of internal waves on a gentle slope in a two-layered system, *Journal of Fluid Mechanics*, 191,
725 419–442, <https://doi.org/10.1017/S0022112088001636>, 1988.
- Walter, R. K., Woodson, C. B., Arthur, R. S., Fringer, O. B., and Monismith, S. G.: Nearshore internal bores and turbulent mixing in southern Monterey Bay, *Journal of Geophysical Research: Oceans*, 117, <https://doi.org/10.1029/2012JC008115>, 2012.

- Winters, K. B.: Tidally driven mixing and dissipation in the stratified boundary layer above steep submarine topography, *Geophysical Research Letters*, 42, 7123–7130, <https://doi.org/10.1002/2015GL064676>, 2015.
- 730 Woodson, C.: The Fate and Impact of Internal Waves in Nearshore Ecosystems, *Annual Review of Marine Science*, 10, 421–441, <https://doi.org/10.1146/annurev-marine-121916-063619>, 2018.
- Wuest, A. and Lorke, A.: Small-scale hydrodynamics in lakes, *Annual Review of Fluid Mechanics*, 35, 373–412, <https://doi.org/10.1146/annurev.fluid.35.101101.161220>, 2003.
- Yih, C.-S.: *Fluid Mechanics-A concise introduction to the theory*, University of Michigan, West River Press, Michigan, USA, Printed in the
735 USA, Card Number 78-65697, 1977.
- Zulberti, A. P., Jones, N. L., Rayson, M. D., and Ivey, G. N.: Mean and Turbulent Characteristics of a Bottom Mixing-Layer Forced by a Strong Surface Tide and Large Amplitude Internal Waves, *Journal of Geophysical Research: Oceans*, 127, e2020JC017055, <https://doi.org/10.1029/2020JC017055>, 2022.